Humidity-Tolerant Moisture-Driven Energy Generator with MXene Aerogel-Organohydrogel Bilayer

Received 00th January 20xx,
Accepted 00th January 20xx

DOI: 10.1039/x0xx00000x

Kaiying Zhao[a,†], Jae Won Lee[a,c,†], Zhi Gen Yu[d], Wei Jiang, Jin Woo Oh, Gwanho Kim, Hyowon Han, Yeonji Kim, Kyuho Lee, Seokyeong Lee, Hoyeon Kim, Taebin Kim, Chang Eun Lee, Hyeokjung Lee, Yong-Wei Zhang[d], Jihye Jang, Jongwoong Park, and Cheolmin Park[a,b]*

High-performance, moisture-driven energy generators (MEG) harness the preferential interaction of ionized moisture with hydrophilic active materials. Free-standing and film-type MEGs are particularly interesting owing to their wearability and portability without needing a water container. However, most MEGs work in limited humidity conditions where moisture is rapidly evaporated from the devices with a high moisture gradient. Herein, we present a high-performance MEG with excellent humidity tolerance and sustainable power-production capability. The demonstrated bilayer-based device comprises a negatively surface-charged, hydrophilic MXene (Ti3C2Tx) aerogel and polyacrylamide (PAM) hydrogel containing ionic salts sandwiched between the top and bottom electrodes. The preferential adsorption on the surface of the highly porous MXene aerogel of positive charges supplied from the salts, and water in the hydrogel, results in high open circuit voltage output when the relative humidity ranges from 20% to 95%. Our MXene aerogel MEG with an active area of 1cm^2 produces a maximum open circuit??? voltage, current density, and power density of approximately 570 mV, 1160 μA/cm^2, and 24.8 μW/cm^2, respectively. y replacing the hydrogel with an organohydrogel of PAM that has excellent water retention and structural stability, a device with long-term electricity generation is realized, which has an output voltage of approximately 320 mV lasting for more than 15 days in a broad temperature range (from –20 to 80 °C). The first principle simulation reveals that the mechanism of MEG originated from the excellent surface charging effect of the cation since the cation has a much lower diffusion energy barrier than the anion, resulting in the separated distribution of cations and anions on the top and bottom of the Mxene surface. Our MXene aerogel MEGs connected in series supply sufficient power for commercial electronic components in various outdoor environments. Moreover, a mechanically flexible, free-standing MXene aerogel MEG can be mounted on the skin for sensitively recognizing finger bending and facial expression changes through the variation of its output current.

[a]*Department of Materials Science and Engineering, Yonsei University, Seoul, 03722, Republic of Korea*

[b]*Spin Convergence Research Center, Korea Institute of Science and Technology (KIST), Seoul 02792, Republic of Korea*

[c]*KIURI Institute, Yonsei University, Seoul, 03722, Republic of Korea*

[d]*Institute of High Performance Computing, Singapore 138632, Singapore*

*Corresponding author address: Department of Materials Science and Engineering, Yonsei University, Seoul, 03722, Republic of Korea

Introduction

Considering the preferential interaction of ions from either moisture or water with various hydrophilic materials, as well as their ion-selective functional groups exposed to the surface, moisture-driven energy generators (MEGs) are a promising technology for next-generation energy conversion.[1-3] The preferential electrokinetic interaction in a MEG occurs during directional moisture evaporation, which spatially dissociates the attractive charges on the surface from the unbound counter-charges, giving rise to the characteristic built-in charge potential.[4, 5] As a pioneering work, Ghosh et al. observed an output voltage between two electrodes placed on carbon nanotubes when water flowed through the nanotube network.[6] Numerous efforts have been made to further facilitate the preferential charge separation in a MEG by developing materials with various surface functional groups,[7, 8] high surface area,[9] and high conductivity.[2] Some examples including surface-functionalized graphene oxides,[10-12] various carbons,[13] polymers,[14, 15] woods,[16] and protein-based biomolecules[17] have been well explored.

Most high-performance MEGs rely on electric power generation, during which active materials are partially immersed in a water reservoir that consistently feeds water molecules into the materials.[18, 19] Owing to the limitations of these so-called liquid-type MEGs in portable and wearable applications, free-standing and film-type MEGs have recently been demonstrated, in which the active materials themselves are capable of absorbing moisture from the environment to efficiently generate electric power, making them potentially suitable as clean electric-power sources for emerging human–machine interface electronics.[16, 20-22] Various self-water-absorbing materials with surface functional groups offering the preferential charge interaction have been demonstrated, such as fluorinated/oxidized graphene foams[7] and poly(vinyl alcohol)-polyamide (PVA-PA) glycerol hydrogels.[21]

Despite great success in developing high-performance, free-standing MEGs with additive salts,[21] gradient materials structures,[1, 20, 21] and device architectures,[23] most of the devices are restricted by a humidity-dependent performance. The devices often operate at a humidity that provides a sufficient moisture gradient to facilitate moisture evaporation from the device to the environment. [24-26] Notably, after water saturation, low humidity favors its high output operation. However, a water-saturated device can rapidly dry out and perform poorly during continuous operation owing to the poor water retention under a low-humidity environment. High humidity can extend its operation time, but the device performance often degrades under higher humidity owing to the slighter moisture gradient. [20] Such humidity intolerance and poor sustainability of the power-generation characteristics of the free-standing MEGs significantly limits their long-term outdoor applications, restricting their use to sunny, dry days.

To address these issues, two materials design strategies were employed in this work. First, we adopted an MEG with a bilayered architecture, where a surface-active material as a power generator was vertically stacked on a hydrogel as a moisture reservoir. In this structure, the moisture gradient inside the device was presumed to be less dependent upon external humidity. Second, we employed an organohydrogel with long-term water-retaining capability and structural integrity to obtain a more suitable MEG for long-term power generation. We also proposed that three-dimensional (3D)-structured MXenes ($Ti_3C_2T_x$) with high electrical conductivity, high surface area, and abundant surface functional groups that provide the preferential charge interaction would be suitable as an active material in our bilayered MEG.[2]

Herein, a high-performance, bilayered MEG with excellent environmental resilience and long-term operation is presented. Our MEG consists of a 3D-structured, negatively charged, hydrophilic MXene aerogel film stacked on a polyacrylamide (PAM) hydrogel containing ionic salts sandwiched between top and bottom electrodes. The positive ions of the ionic salts and water supplied from the PAM hydrogel by capillary action dissociate and preferentially absorbed on the surface of the highly porous MXene aerogel, giving rise to high electric output over a wide range of external humidity (i.e., 20–95%). Our MXene aerogel-on-hydrogel MEG (MAH-MEG) with an active area of 1 cm^2 exhibits a maximum output open-circuit voltage (V_{oc}), short-circuit current density (J_{sc}), and power density of approximately 570 mV, 1160 μA/cm^2, and 24.8 μW/cm^2, respectively. Furthermore, an MXene aerogel-on-organohydrogel MEG (MXO-MEG), which combined a highly water-retentive, structurally stable PAM organohydrogel with an MXene aerogel, demonstrated highly sustainable electricity generation (≈320 mV) lasting for more than 15 days. Our MXO-MEG consistently performed well in a humidity range of 20–95% and temperature range between –20 and 80 °C, making it suitable as a portable and wearable power generator for various commercial electronic components subjected to a broad range of outdoor environments. Moreover, when mounted on human skin, the mechanically flexible, free-standing MXO-MEG successfully recognized finger bending as well as facial expression changes by sensitively varying its output current.

Results and discussion

Fabrication of MAH-MEG

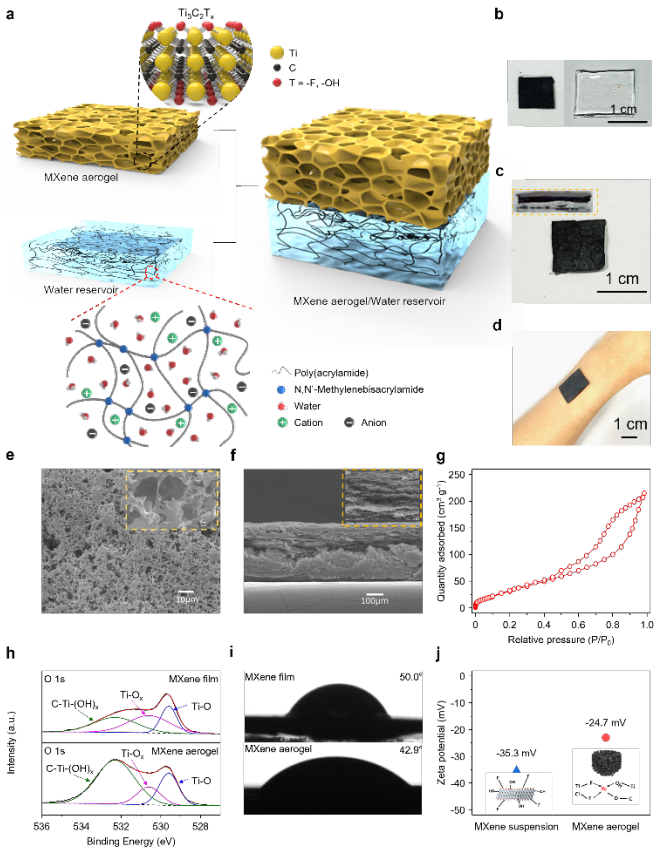

Figure 1. 3D-structured bilayer MAH-MEG. (a) 3D schematic showing the structure and fabrication process of the MAH-MEG device. (b) Top view of the MXene aerogel and PAM ionic hydrogel, (c) top and side views of the MAH-MEG, and (d) photo of the device attached to human skin. (e) Top and (f) cross-sectional SEM images of the MXene aerogel. g) N_2 adsorption/desorption curves of the MXene aerogel. (h) O 1s XPS spectra and (i) contact angle of the MXene film and aerogel. (j) Zeta potential of the original MXene suspension and MXene aerogel.

Schematics of the fabrication of the MAH-MEG are shown in Figure 1a, and the details are given in the Methods section. The free-standing MXene $Ti_3C_2T_x$ (T = F, O, or OH) aerogel was prepared by freeze-drying gelated MXene suspension after vacuum filtration (Figure S1, Supporting Information).[27] The highly flexible PAM ionic hydrogel used as a film-type water reservoir was formed under free-radical polymerization and then drop-casted at 60 °C.[28] The thickness of the obtained ionic hydrogel was ≈1 mm. Figure 1b shows photographs of the MXene aerogel and PAM ionic hydrogel viewed from the top, and Figure 1c shows top and side views of the MAH-MEG. The detailed device-fabrication processes are provided in Figure S2 of the Supporting Information. In short, the bottom electrode was stuck to a poly(ethylene terephthalate) (PET) substrate, followed by sequential deposition of the PAM hydrogel, MXene aerogel, and top electrode. The sticky hydrogel was easily attached to human skin, as shown in Figure 1d. Figures 1e and f show the top and cross-sectional scanning electron microscope (SEM) images of the bilayered MXene aerogel, respectively. The 3D-structured MXene aerogel contains numerous irregular holes and micro/nanoscale channels that act as moving passes for ions. SEM images of the PAM hydrogel and the device are also shown in Figure S3 of the Supporting Information.

Figure 1g shows the N_2 adsorption/desorption curves of the MXene aerogel, which indicate an inhomogeneous porous structure with a surface area of ≈105 m^2/g. The O 1s and C 1s X-ray photoelectron spectra were acquired, as shown in Figures 1h and S4 of the Supporting Information. Their chemical states were obtained by fitting the corresponding spectra (Table S1, Supporting Information). An MXene film contains abundant oxygen and fluorine terminations, as evidenced by the O/C ratio of 0.29 and O/Ti ratio of 0.64. Interestingly, the O/C (0.48) and O/Ti (0.77) ratios in the MXene aerogel were higher than those in the MXene film, indicating an increase in the amount of oxygen functionalities during the aerogel foaming process. Moreover, in the XPS O 1s spectrum of the MXene aerogel (Figure 1h), the peak corresponding to C–Ti–$(OH)_x$ at 532.2 eV was much stronger than that of the MXene film, corroborating the formation of terminal oxygen-containing functional groups in the former.

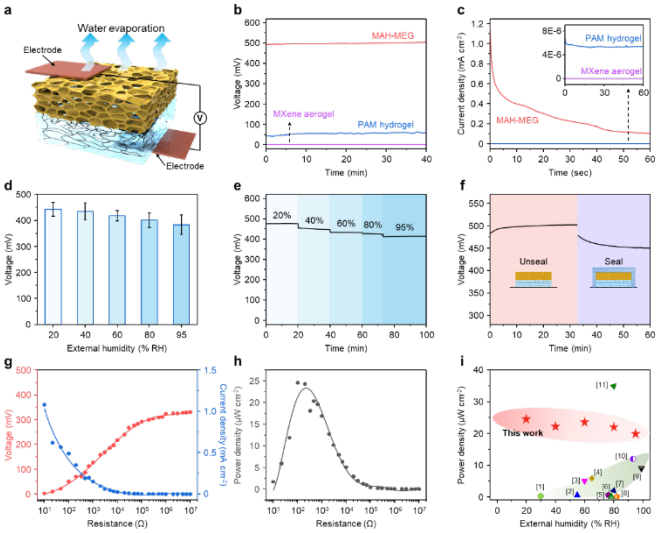

Figure 2. Electric power generation of the humidity-tolerant MAH-MEG. (a) Schematic of power generation under ambient conditions. (b) V_{oc} and (c) J_{sc} of Cu/MXene aerogel/Cu, Cu/PAM hydrogel/Cu, and the MAH-MEG. (d) V_{oc} and (e) continuous voltage output of the MAH-MEG as a function of RH. (f) V_{oc} produced when the device is unsealed and sealed in humid environment. (g) V_{oc} and J_{sc} of the MAH-MEG as a function of external load from 10 Ω to 10 MΩ at 20% RH. (h) Power density obtained by measuring the V_{oc} and J_{sc} according to (g). (i) Comparison of the performances of recently reported MEGs with those of the MAH-MEG produced in this work according to humidity. [7,17,21,22,33-39]

Meanwhile, the increased intensities of the peaks corresponding to C–O bonds (286.4 eV) and C=O bonds (288.6 eV) confirmed this result (Figure 1h and S4 of the Supporting Information). The contact angles of the MXene aerogel and film were compared, and the results are shown in Figure 1i. Noticeably, the contact angle of the MXene aerogel (θ = 42.9°) is smaller than that of the film (θ = 50.0°); thus, the MXene aerogel has a more hydrophilic surface. The hydrophilic MXene

aerogel functioned as an active material with a zeta potential of –24.7 mV, which is slightly higher than that of the original MXene suspension (–35.3 mV) (Figure 1j). This increase is due to the introduction of a small number of ferrous ions (Fe^{2+}) during gelation.[27] Owing to the negative zeta potential of the MXene aerogel, the ions in the PAM hydrogel are separated at the interface with the MXene aerogel, giving rise to an electrical potential.

Humidity-tolerant electric power of MAH-MEG

Power generation of an MAH-MEG composed of Cu top and bottom electrodes was tested under ambient conditions with various external humidity conditions, as shown in Figure 2a. Prior to testing of the MAH-MEG, two control devices, Cu/MXene aerogel/Cu and Cu/PAM hydrogel/Cu were tested, corresponds to Figure 2b and c. Neither V_{oc} nor the short-circuit current (I_{sc}) was observed in the Cu/MXene aerogel/Cu device owing to the absence of a moisture gradient. For Cu/PAM hydrogel/Cu, V_{oc} and I_{sc} were measured to be approximately 75 mV and 70 nA, resulting from the charge separation in the hydrogel during the directional evaporation of water from the bottom to top surface, as reported in previous works.[29,30] Interestingly, in our MAH-MEG, in which a piece of MXene aerogel was stacked on the PAM hydrogel, the V_{oc} rapidly increased to ≈500 mV with a significantly enhanced I_{sc} of ≈1160 μA, as shown in Figure 2c. The results clearly show the effectiveness of the stacked device structure on power generation.

Next, to investigate the role of the microporous MXene aerogel, we fabricated another control device composed of a bilayer comprising an MXene film and PAM hydrogel. The MXene film was prepared by drop-casting the same amount of MXene suspension used for the MXene aerogel (5 mL) on a filter paper, followed by thorough drying of the film. The MXene film consists of stacked MXene flakes aligned parallel to the film surface (Figure S5, Supporting information). The MXene film on the MEG hydrogel (MFH-MEG) also exhibited excellent power-generation performance, with a V_{oc} and I_{sc} of approximately 380 mV and 180 μA, respectively (Figure S6, Supporting information). However, both values are lower than those of the MAH-MEG. Notably, the I_{sc} value of the MAH-MEG was more than six-fold higher than that of the MFH-MEG. We believe that the enhanced device performance was mainly due to the characteristic porous structure of the MXene aerogel, which facilitates ion movement. Owing to the porous structure of the MXene aerogel, it was ≈400 μm thick, which is significantly thicker than an MXene film (20 μm) (Figure S5, Supporting information).

The external humidity significantly affects the performance of the film-type MEG. High humidity is often initially required to supply sufficient moisture to the device. [21,31,32] Once a device is saturated with water, its power-generation performance is also significantly affected by the external humidity at which power generation occurs. In other words, upon saturation of the device, its performance degrades with increasing external humidity because the moisture gradient decreases. At a relatively low external humidity, a large moisture gradient builds between the highly moisture-saturated device and the low-humidity environment, giving rise to high device performance. However, when a device is exposed for long periods to a relatively low humidity, the device performance rapidly declines owing to the lack of water retention capability.

To assess the humidity-dependent power generation of a MEG, we exposed the MAH-MEG to a wide range of relative humidity ranging from 20% to 95%, as shown in Figure 2d. Notably, a PAM hydrogel in the MAH-MEG was initially saturated with water when prepared. Our MAH-MEG exhibited the highest V_{oc} of ≈450 mV at 20% relative humidity (RH). Surprisingly, the decrease in the V_{oc} of the device with increasing humidity was marginal, changing by only ≈50 mV (only 10% of the initial 450 mV V_{oc}) upon humidity variation from 20% to 95%.

The V_{oc} of the device was continuous measured over time while maintaining each external humidity condition for 20 min. The V_{oc} dropped from ≈470 mV at 20% RH to ≈420 mV at 95% RH after 100 min of continuous operation, as shown in Figure 2e. The humidity tolerance of our MAH-MEG arises from its unique device architecture, comprising a vertically stacked bilayer of an MXene aerogel and PAM hydrogel. Unlike most film-type MEGs, where charge separation and migration occur in a single film capable of absorbing moisture, [2,21] our MAH-MEG consists of two independent layers of MXene aerogel and PAM hydrogel for water absorption and charge separation and migration, respectively. We speculate that the internal moisture gradient in the MAH-MEG is much less affected by the external humidity.

To support our hypothesis that the moisture gradient in in the MAH-MEG is less sensitive to external humidity, we examined an MAH-MEG device entirely sealed with commercial tape to isolate it from external humidity; the results are shown in Figure 2f. Again, the V_{oc} of the sealed device decreased only marginally, that is, to a value less than 10% that of the unsealed device, confirming that the external humidity barely affects the device performance. These results corroborate the existence of an internal moisture gradient in the MAH-MEG. The marginal output variation with the restriction of moisture evaporation was also confirmed when inverting the MAH-MEG. In this case, the MXene aerogel faced an impermeable substrate (Figure S7, Supporting Information). Notably, the MAH-MEG gave a negligible V_{oc} when the PAM hydrogel was completely dried. The V_{oc} of the device was developed by uptaking water under different humidity conditions, making our MAH-MEG reusable after repetitive dry–wet cycles (Figures S8, Supporting Information).

The power densities of the MAH-MEG devices were obtained by measuring the V_{oc} and J_{sc} as a function of external loads from 10 Ω to 10 MΩ, as shown in Figures 2g and 2h. The equivalent-test-circuit diagram is shown in Figure S9 of the Supporting Information. The V_{oc} significantly increased with increasing resistance, whereas the output J_{sc} decreased. At 150 Ω, the maximum power density of 24.8 μW/cm^2 was obtained at a 20% RH. We also evaluated the power densities of the device as a function of external humidity from 20% to 95%. The external-

humidity-dependent power densities of the device were compared with those of recently reported MEGs, as shown in Figure 2i. [7, 17, 21, 22, 27-33] Most previously reported MEGs demonstrated a reasonable power density when exposed to a high-humidity environment (usually >60% RH). Their performances significantly diminished when placed in low-humidity environments (<60% RH). However, in the case of the MAH-MEG, high power densities were reliably generated under a wide range of humidity conditions (20–95% RH). The performance of our MAH-MEG was also compared with those of MEGs based on MXenes (Table S2, supporting information).[2, 32, 34-37] A more comprehensive comparison of the performance of the MAH-MEG prepared using the portable MEGs clearly demonstrates its superior humidity tolerance (Table S3, Supporting Information).

Working mechanism of MAH-MEG

In our MAH-MEG, directional moisture evaporation occurred from the bottom to top of the MXene aerogel stacked on the PAM hydrogel, which contained abundant Ca^{2+} and Cl^- ions dissolved in water. Owing to the presence of various functional groups on the surface of the MXene, such as oxygen (–O), fluorine (–F), hydroxyl (–OH), and chlorine (–Cl), our MXene aerogel is hydrophilic with a characteristic negative zeta potential.[38] Therefore, the channels in the MXene aerogel can be hydrolyzed to appear negatively charged when water infiltrates the channels. The hydrophilic groups on the MXene aerogel allow the film to absorb electrolytes from the ionic hydrogel. Simultaneously, a negatively charged surface repels anions. The negatively charged nanochannels repel negatively charged ions (OH^- and Cl^-) but allow the positively charged ions (H_3O^+ and Ca^{2+}) to pass through,[2, 18] inducing a streaming potential and charge accumulation along with a flow that forms an electric field (Figure S10, Supporting Information).[20] Thus, a diffusion current is formed from bottom to top. Without connection to an external circuit, the channel would generate a corresponding electric field (creating a drift current with the internal resistance of the MXene aerogel) to balance the diffusion current. When an external circuit is connected, the drift current generated by balancing the diffusion current in the film correspondingly decreases, and the external circuit balances the remaining diffusion current, thereby generating a drift current through the external resistor. Continuous water evaporation at the film–air interface and continuous water supply at the aerogel–hydrogel interface provide constant energy input. The electricity generation mechanism is illustrated in Figure 3a.

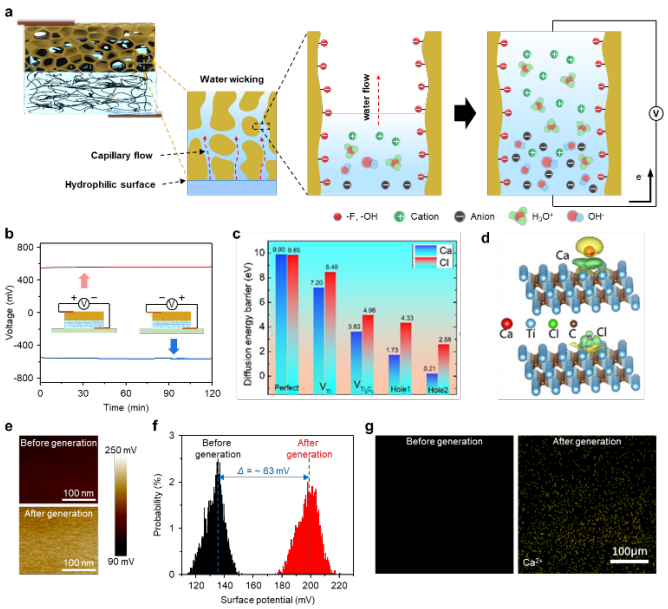

Figure 3. Working mechanism of MAH-MEG. (a) Schematic of the electricity-generation mechanism. (b) Polarity test of the MAH-MEG device. The sign of the induced voltage is reversed upon reversing the source-meter electrodes. (c) The calculated diffusion barriers of Ca and Cl ions in different configurations (left panel) and the charge density difference of Ca and Cl ions on the pristine Ti_3C_2 surface (right panel). The yellow and green colour represent the electron depletion (anti-bond states) and accumulation (bonding states), respectively. (d) KPFM images and (e) surface-potential changes of MXene aerogel before and after moisture-driven power generation. (f) EDS mapping of a pristine MXene aerogel (left) and an MXene aerogel combined with a salt-ion-containing PAM hydrogel after moisture-driven power generation (right).

Recently, the electrodes have also been found to affect MEG devices.[19] However, the effect of active electrodes on power generation seems to be overlooked in the most recent research. We examined MAH-MEGs with different contact electrodes composed of metals such as Cu, Ag, and Au, and the results are shown in Figure S11a of the Supporting Information. An MAH-MEG with Au top and bottom electrodes exhibited a V_{oc} and I_{sc} of approximately 140 mV and 5 μA, respectively (Figures S11b and S11c, Supporting Information). When Ag electrodes were employed, the device exhibited a V_{oc} and I_{sc} of approximately 250 mV and 170 μA, respectively (Figure S11a, Supporting Information). The performance of MAH-MEGs with Au and Ag electrodes is poorer than that of the device containing Cu electrodes. This result suggests that in addition to the power generation of an MAH-MEG arising from the proposed interaction of the MXene aerogel and water containing salt ions, an additional principle governs power production when Cu electrodes are used.[16] The cyclic voltammetry (CV) curve for the device with Cu electrodes contained a characteristic redox peak (Figure S12, Supporting Information). When the Cu cathode and anode are connected to the external circuit, the oxidation of Cu releases Cu^{2+} and electrons at the anode, and the moisture and oxygen adsorbed on the cathode side of the MXene aerogel accept electrons to form OH^-. The OH^- subsequently migrates to the anode and combines with Cu^{2+} to form $Cu(OH)_2$. The reactions at the cathode and anode of the MAH-MEG can be expressed as follows[16]:

Cathode: $O_2 + 2\ H_2O + 4\ e^- \rightarrow 4\ OH^-$

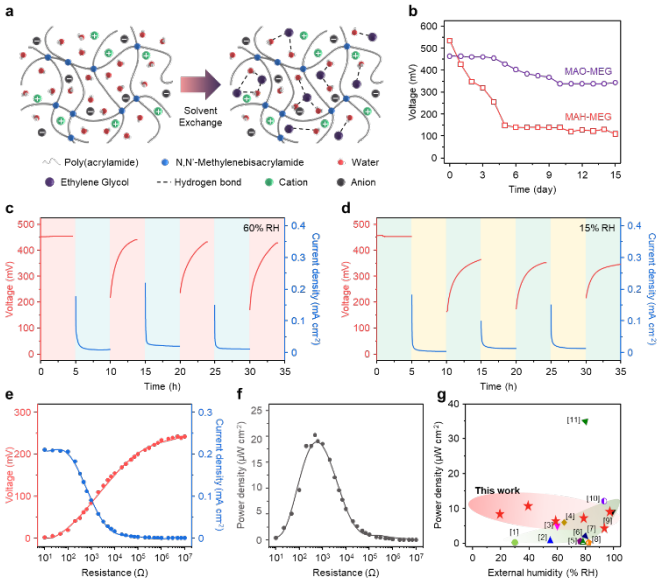

Figure 4. Sustainable power generation of the MAO-MEG. (a) Schematic of hydrogel replacement by the organohydrogel through a solvent-exchange process. (b) Long-term V_{oc} testing of MAH-MEG and MAO-MEG at 20% RH. The discharging and charging properties of the MAO-MEG at (c) 60% and (d) 15% RH. The V_{oc} (red) and J_{sc} (blue) from the working MAO-MEG with continuous measurement. (e) The V_{oc} and J_{sc} of the MAO-MEG as a function of external loads from 10 Ω to 10 MΩ at 20% RH. (f) Power density obtained by measuring the V_{oc} and J_{sc} according to (e). (g) Comparison of the performances of the MAO-MEG designed in this work with those of recently reported MEGs according to humidity. [7,17,21,22,33-39]

Anode: $2\ Cu - 4\ e^- \rightarrow 2\ Cu^{2+}$

Overall cell reaction: $2\ Cu + O_2 + 2\ H_2O \rightarrow 2\ Cu(OH)_2$

However, when the device was tested in different atmospheres (air and N_2), there was no major difference in the electrical output (Figure S13, Supporting Information). In addition, after the device was placed in water, the voltage began to decrease gradually; after 12 h, only 70 mV remained (Figure S14, Supporting Information). This is because the humidity gradient is gradually destroyed upon soaking the device. From these results, we believe that the internal gradient structure is the most important factor in electricity generation, while the redox reaction contribution to electric output is less important.

The MXene side of the MAH-MEG always has a higher potential, as shown in Figure 3b. When the positive electrode of the testing circuit is connected to the top electrode of the MAH-MEG, the voltage is positive. The polarity of the V_{oc} changed (with the same absolute value) when the positions of the positive and negative electrodes were reversed, further confirming the proposed working mechanism of the development of electric potential between the MXene aerogel and PAM hydrogel.

To gain an in-depth understanding of the mechanism of MAO-MEG, we performed the first principles simulation on $CaCl_2$ embedded Mxene (Ti_3C_2) based on the density functional theory (DFT). First, we focused on the perfect Ti_3C_2 system. We investigated native defects in monolayer Ti_3C_2. Here, we only considered Ti vacancy (V_{Ti}) and C vacancy (V_C), and the calculated formation energies are shown in the right panel of Figure S15 and the relative configurations are shown in the left panel. It should be noted that there are two types of Ti vacancy in Ti_3C_2. Based on the calculated formation energy, it can be seen that V_{Ti2} has the lowest formation under the Ti-rich growth condition, while V_C has the lowest formation energy under the Ti-poor growth condition. Therefore, the complex defects containing V_{Ti} and V_C were considered in the following study of Ca and Cl ions diffusion barriers. Here, we mainly focused on Ca and Cl ions diffusion in Ti_3C_2. Based on the structure of Ti_3C_2 Mxene and our experimental devices structure, two diffusion pathways shown in Figure S16a, vertical (crorssing layer) and horizontal (inter-layer) were considered in our DFT study.

Starting from the pristine T_3C_2 Mxenes, shown in Figure S26b, we computed the diffusion energy barriers of Ca and Cl ions are 9.90 eV and 9.85 eV shown in Figure 3c. Not surprisingly, Ca and Cl ions may not cross the Ti_3C_2 Mxenes layer. Based on our device's structure delivering an inhomogeneous porous structure and defect formation energy, we consider four complex defects in Ti_3C_2 Mxenes. They are V_{Ti} ,$V_{Ti_3C_2}$ hole 1 and hole 2 shown in Figure S16c-f. The calculated diffusion barriers are shown in Figure S17b-e, and the summarized energy barriers are shown in Figure 3c. The diffusion barriers of Ca and Cl are 7.20 eV and 8.48 eV with introducing V_{Ti}, respectively. The diffusion barriers of Ca and Cl significantly decrease to 3.63 eV and 4.96 eV with $V_{Ti_3C_2}$, and further reduce to 1.73 eV and 4.33 eV with hole 1 configuration, respectively. We further increased the size of hole and expanded to hole 2 configuration, and the computed diffusion barriers of Cal and Cl shown in Figure 3 (right panel), are 0.21 eV and 2.58 eV, respectively. Based on our DFT simulation results, we consider that Ca^{2+} ions may cross the T_3C_2 Mxenes layer toward the top surface through the self-diffusion, and Cl ions may freeze at the interfacial between MXene aerogel and PAM hydrogel. Meanwhile, we also demonstrate that a bigger hole is beneficial for Ca ion diffusion and make the device rapidly realize the stable open circuit voltage.

We further investigated the diffusion barriers of Ca and Cl ions on the surface shown in Figure S18, and the results are shown in Figure S27f. The calculated diffusion barriers of Ca and Cl ions are 0.003 eV and 0.239 eV, respectively. The results reveal that Ca has a tiny interaction with Ti_3C_2 Mxenes layer, and Ca^{2+} ions are mobile and form uniform distribution on the surface, resulting in an excellent surface charging effect and long-term stable power output. The calculated charge density difference of Ca (Cl) and Ti_3C_2 Mxenes layer is shown in Figure 3d. It can be seen that most electrons accumulate (green) and depletion (yellow) nearby the Ca ion, and Ca ion has no electron exchange with the Mxene surface. The result reveals no chemical bonds between Ca and Ti_3C_2 Mxenes, which is consistent with the ultra-low diffusion barrier of Ca ion (0.003 eV) on the Ti_3C_2 Mxenes surface. For the Cl ion, all electrons accumulate around the Cl ion, and the electron accumulation is much stronger than the electron depletion, revealing the bonding states are more than the anti-bonding states resulting in the strong chemical bond between Cl and Ti. It is well known that the Ti_3C_2 Mxenes surface is saturated by Cl, O and OH ions. The DFT results are consistent with our experimental observation, in which it was found that a concentration gradient of Ca^{2+} ions exists from the bottom to the top on the aerogel surface.

Furthermore, a Kelvin probe force microscope (KPFM) was used to probe the potential change of the MXene aerogel surface before and after moisture-wicking, as shown in Figure 3e. The surface potential increases from ≈135 to ≈198 mV after moisture-wicking owing to the accumulation of positive charge carriers (Figure 3f).Figure 3g shows the cross-sectional energy-dispersive X-ray spectroscopy (EDS) map of a pristine MXene aerogel (left) and an MXene aerogel with a PAM hydrogel containing salt ions after moisture-driven power generation (right). The EDS map of the pristine MXene aerogel that was not subjected to power generation reveals no traces of Ca^{2+} ions. After generating an output voltage, a substantial amount of Ca^{2+} ions were produced, as shown in the image on the right side of Figure 3f. A concentration gradient of Ca^{2+} ions extending from bottom to top is visible on the aerogel surface. More details on the EDS mapping procedure are given in Figure S19 of the Supporting Information. A similar concentration gradient of Na^{+} ions was observed in the EDS map of the MAH-MEG incorporating NaCl (Figure S20, Supporting Information). The development of a vertical electrical potential between the MXene aerogel and PAM hydrogel was also confirmed in the experiment examining the power generation of MAH-MEGs with different locations of the electrodes. The devices with two electrodes connected to the MXene aerogel and PAM hydrogel exhibited almost identical V_{oc} regardless of the lateral locations of the electrodes on both films (Figure S21, Supporting Information).

Sustainable power generation with organohydrogel

Long-term water retention of a hydrogel is essential for sustainable power generation of an MEG, particularly at low humidity. Despite the excellent performance of the MAH-MEG, the water-retention properties of the PAM hydrogel need to be improved because the hydrogel easily loses water in a low-humidity environment over time, rapidly degrading the device performance. To address the issue, we incorporated an organohydrogel with excellent water retention capability into an MEG suitable for sustainable power production.[39] As can be seen in Figure 4a, the water-retention performance of this device is better. An organohydrogel was obtained by replacing part of the water in the hydrogel with organic solvents; to accomplish this substitution, we soaked a PAM hydrogel in ethylene glycol for at least two hours. The water retention of the organohydrogel was examined by comparing its weight after a particular time to its initial weight, yielding a ratio (Figure S22a, Supporting Information). Even after 6 days at 20% RH, the weight of the organohydrogel barely decreased (from 100% to 99.8%); after 15 days, the weight decreased to ≈87.9% of its initial weight. On the contrary, after 2 days at 20% RH, the PAM hydrogel was reduced to 70% of its initial weight, further diminishing to ≈46.2% after 15 days (Figure S22b, Supporting Information). Under low-humidity conditions, the PAM hydrogel rapidly shrunk over time, leading to the precipitation of salts in the hydrogel owing to water loss, while the organohydrogel remained transparent and in good shape.

The evolution of the V_{oc} of an MXene aerogel-on-organohydrogel MEG (MXO-MEG) with time was examined at 20% RH, and the results are shown in Figure 4b. Compared with the performance of an MAH-MEG, the initial V_{oc} of ≈450 mV was slightly lower, mainly owing to the low solubility of the salt ions in the organic solvent. Surprisingly, the V_{oc} of the MXO-MEG was maintained for over 15 days, slightly decreasing to ≈350 mV. On the other hand, the initial V_{oc} of ≈540 mV for the MAH-MEG rapidly decreased to ≈100 mV. The J_{sc} for the MAO-MEG was also maintained (Figure S23, Supporting Information).

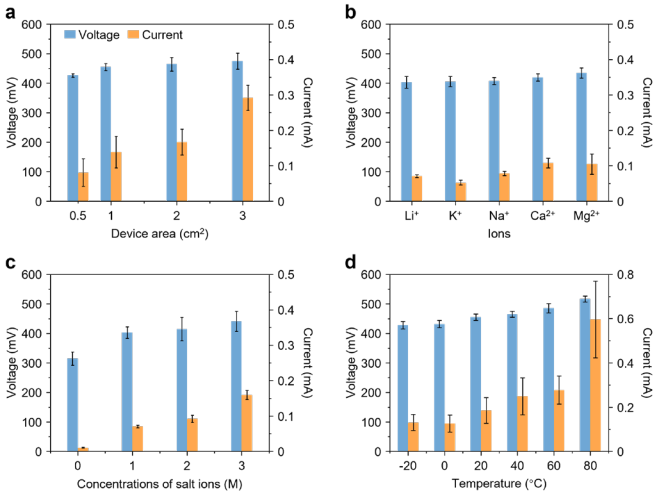

Figure 5. Factors influencing the power-generation performance of MAO-MEGs. (a–d) V_{oc} and I_{sc} of MAO-MEG devices with different (a) areas, (b) cations, (c) concentrations of salt ions, and (d) temperatures at 20% RH.

In addition, we investigated the discharging and charging properties of an MAO-MEG at 60% and 15% RH; the results are shown in Figures 4c and 4d, respectively. When the device was discharged with an initial V_{oc} of ≈400 mV (the leftmost blue curve in Figure 4c) at 60% RH, the voltage of the device decreased to ≈200 mV (the second-left red curve in Figure 4c). The V_{oc} was restored to its original value (≈400 mV) after self-charging for five hours, readying it for another current discharge. The MAO-MEG could be self-discharged and repeatedly charged, similarly to the recently reported hydrogel-based devices.[20, 21] More interestingly, the MAO-MEG exhibited excellent discharging and charging performance, even at a low humidity of 15% RH, as shown in Figure 4d. Although the restored V_{oc} of the device after discharging (≈350 mV) was slightly lower than the initial voltage (≈450 mV), repetitive charging and discharging were achieved with time. As expected, the performance of the MAH-MEG device charged and discharged at 60% RH (Figure S24a, Supporting Information) was very poor at 15% RH owing to substantial water loss of the PAM hydrogel (Figure S24b, Supporting Information). The performance of our oraganohydrogel-containing MAO-MEG clearly demonstrates its potential as a highly sustainable energy harvester.

The power densities of the MAO-MEG were evaluated by connecting the device to various external resistors. From the resistance-dependent V_{oc} and J_{sc} values (Figure 4e), the power densities of the device were obtained as a function of resistance, as shown in Figure 4f. The power density of ≈8.3 μW/cm² was obtained at a resistance of 1000 Ω, even at 20% RH. The power densities of the device were also evaluated as a function of humidity, and the results in Figure 4g indicate that our MAO-MEG is also humidity tolerant, with a maximum power density of ≈10 μW/cm² at 40% RH. Compared with the MEGs reported in recent publications, [7, 17, 21, 22, 27-33] our MAO-MEG is outstanding owing to its long-term power-generation capability, particularly in low-humidity conditions.

Factors influencing the power-generation performance of MAO-MEGs

First, we examined the performance of the MAO-MEG as a function of device size; the results are shown in Figure 5a. MAO-MEGs with

active areas of 0.5, 1, 2, and 3 cm^2 were tested. The results show that while the V_{oc} values of the devices barely varied with the device size, the I_{sc} values linearly increased with the device size, which is consistent with the theoretical prediction of the ion-based surface-charging effect.[26] We also investigated the effect of salt ions on device performance.[2,42] The negatively charged surface of the MXene ($Ti_3C_2T_x$) sheets induces a high affinity toward both monovalent and divalent cations and promotes the build-up of electrical double layers.[2] Conventional electrolyte solutions with cations such as Li^+, K^+, Na^+, Ca^{2+}, and Mg^{2+} were incorporated into the organohydrogels of the MAO-MEGs, as shown in Figure 5b. All the devices exhibited excellent V_{oc} and I_{sc} values.

The effect of the salt-ion concentration on both the V_{oc} and I_{sc} of an MAO-MEG was also examined, and the results are shown in Figure 5c. When the concentration was increased, both the V_{oc} and I_{sc} increased owing to the higher charge density in the electrical double layer. In addition to the humidity tolerance of the MAO-MEG, its operation in a wide temperature range would also be beneficial, allowing the device to be used in various environmental conditions. Our MAO-MEG performed well over a broad range of temperatures (i.e., from –20 to 80 °C), as shown in Figure 5d. In fact, both the V_{oc} and I_{sc} values slightly increased with temperature mainly owing to facilitated sorption and diffusion of ions in the device.[1, 40] In particular, I_{sc} substantially increased at 80 °C. Notably, owing to the anti-freezing characteristics of the organohydrogel, our MAO-MEG device functioned properly even at –20 °C, which is far below the freezing temperature of water. The device could be continuously operated despite in-situ temperature changes by using a heating light bulb (Figure S25 and Movie S1, Supporting Information). The V_{oc} and I_{sc} immediately increased each time the light bulb was turned on to heat the device.

The effect of the thickness of both the hydrogel and MXene aerogel on the performance of the MAO-MEGs was also thoroughly investigated (Figure S26-28, Supporting Information). The device performance was enhanced when the hydrogel layers at a given MXene aerogel were thicker, apparently owing to the higher amount of water and salt ions in the device. The device performance degraded when the MXene aerogel surpassed its critical thickness owing to increased ion diffusion, which is consistent with the findings of previous works.[26] The device performance could also be enhanced by increasing the area of the MXene aerogel at a given thickness (Figure S29, Supporting Information).

Scalability of MAO-MEG and its applications

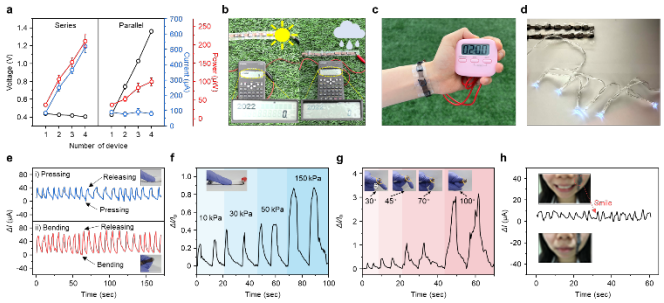

Figure 6. Scalability of MAO-MEG and its applications. (a) Plot of V_{oc} and I_{sc} with different numbers of MAO-MEG units connected in series and in parallel. (b) Photographs of a commercial calculator operated on sunny and rainy days using seven MAO-MEGs units connected in series. (c) Photograph of a commercial watch operated using a wristband harvester. (d) Photograph of six LEDs simultaneously turned on by a power harvester consisting of 20 MAO-MEGs units connected in series. (e) Current variations of the self-powered wearable sensors in response to pressing the finger on a surface and bending the finger joint. Current response to different (f) pressures and (g) bending angles. (h) Current response to smiling when the device is mounted on the cheek.

Our humidity- and temperature-tolerant MAO-MEG with high-power density and wearability can be readily hybridized or integrated into humans' daily lives.[4, 27] Depending on the application, the size and number of mechanically flexible and lightweight MAO-MEG units were varied to provide sufficient power. By connecting four MAO-MEGs in parallel for demonstration, the integrated array produced more than quadruple the current of a single unit. The V_{oc} of the arrays remained nearly the same as that of a single unit, as shown in Figure 6a (left). When the four units were arranged in a series, the connected arrays' V_{oc} was four-fold greater than that of a single unit. By contrast, the current of the arrays was unaltered, as shown in Figure 6a (right). The various combinations of the MAO-MEGs in series were examined, allowing for facile control of the V_{oc} (Figure S30, Supporting Information). By connecting seven units of the environmentally tolerant MAO-MEGs in a series, a commercial calculator was successfully operated on sunny, hot days as well as rainy ones, as shown in Figure 6b. By harnessing the mechanical flexibility and wearability of the MAO-MEGs, we fabricated a power-harvesting wristband by connecting seven MAO-MEG units in a series, as shown in Figure S30b, Supporting Information. The wristband harvester could operate a commercial watch worn on the wrist, even at 27% RH (Figures 6c). In addition, six LEDs were simultaneously turned on by a power harvester consisting of 20 MAO-MEG units connected in a series, as shown in Figure 6d.

Moreover, our MAO-MEG was employed as a self-powered wearable sensor; the results are shown in Figures 6e–h. Hydrogel-based nanogenerators are very sensitive to externally applied pressure and are often used as wearable sensors.[41] Therefore, our MAO-MEG is beneficial because the device containing the organohydrogel provides sustainable electric power for sensor operation. When a gentle pressure was applied to the surface of an MAO-MEG, the I_{sc} of the device instantly increased to ≈40 μA, as shown in Figure 6e (top). When the pressure was stopped, the initial I_{sc} was re-established. The I_{sc} variation of the device upon the application of pressure was repetitive. Similarly, an MAO-MEG was successfully patched on the finger joint using a commercial adhesive, as shown in the photo in the inset of Figure 6e (bottom). When the finger wearing the device was bent, the I_{sc} increased to ≈60 μA owing to the compression of the device upon bending, as shown in Figure 6e (bottom). The repetitive bending motions of the finger were accurately reflected in the I_{sc}. The I_{sc} variations of the sensor upon the application of different pressures and bending

angles are shown in Figure 6f and 6g, respectively. The sensitivity of the pressure sensor is displayed in Figure S31, Supporting Information. Furthermore, our self-powered, pressure-sensitive MAO-MEG could be readily attached to the cheek, as shown in the photographs in Figure 6h. The change in facial expression upon smiling caused compression of the device, increasing the I_{sc}, as shown in Figure 6h. Once again, repetitive smiles were precisely reflected in the I_{sc} change of the device.

Conclusions

In summary, we developed a high-performance bilayered MEG with excellent environmental tolerance and long-term operation. Our MAH-MEG incorporates a hydrophilic, negatively charged MXene aerogel and a PAM hydrogel-supplied water and performs a maximum V_{oc}, J_{sc}, and power density of approximately 570 mV, 1160 μA/cm^2, and 24.8 μW/cm^2, respectively. The internal moisture gradient in the power-generation layer of the highly porous MXene aerogel is much less affected by the external humidity, making its performance reliable. Furthermore, highly sustainable electricity generation of ≈320 mV was achieved for more than 15 d using an MXO-MEG combining an MXene aerogel with a PAM organohydrogel with excellent water retention and structural stability. Our MXO-MEG performs consistently well under relative humidity ranging from 20% to 95% and in the temperature range from –20 to 80 °C, making it amenable to portable and wearable power generation in a broad range of outdoor environments. The DFT results reveal that the excellent surface charging effect originates from the separation of cations and anions. Moreover, our mechanically flexible, free-standing MXO-MEG mounted on the skin is promising for detecting finger bending and changes in facial expression by measuring its I_{sc}. This work provides a reference for future studies on the functionality of MEGs under a broad range of humidity. It also expands the application of MXene aerogels and hydrogels in this field.

Methods

Materials. Acrylamide, *N*,*N*'-methylene bisacrylamide (MBAA), ammonium persulfate (APS), *N*,*N*,*N*',*N*'-tetramethylethylenediamine (TEMED), ethylene glycol, $CaCl_2$, LiCl, $MgCl_2$, KCl, NaCl, and $FeCl_2{\cdot}4H_2O$ were purchased from Sigma-Aldrich. The MXene suspension (10 mg/mL) was purchased from XinXi Tchnology Co., Ltd. (Foshan, China).

Fabrication of MXene aerogel. In a typical gelation process, 40 mg $FeCl_2{\cdot}4H_2O$ powder was dissolved in 0.2 mL of deionized (DI) water, followed by adding 5 mL of MXene suspension (10 mg/mL); the MXene gel was formed within a few seconds.[42] Then, 50 mL of DI water was added to the MXene gel and shaken for dozens of seconds. The resulting suspension was filtered through a cellulose acetate membrane (0.2 μm pore size and 47 mm diameter) and freeze-dried (Freeze dryer, FDS 8512, Ilshinbiobase).[43]

Preparation of PAM hydrogel and organohydrogel. As per convention, 7.71 g of the acrylamide monomers were dissolved in 50 mL DI water under magnetic stirring, followed by the addition of 0.03 g of MBAA and 0.08 g of APS. $CaCl_2$ was dissolved in 2 mL of as-prepared solution to obtain a solution of 1–3 M. Five microliters of aqueous TEMED (2.5 wt%) were added as the cross-linking accelerator. The prepared solution was drop-casted in a mold with the desired dimensions and then cured at 60 °C.[44] The viscous polyacrylamide solution gradually lost its liquidity, producing a highly stretchable hydrogel in the process. To prepare the organohydrogel, the neat hydrogel was soaked in ethylene glycol for at least two hours to promote solvent exchange.[45,39]

Fabrication of the MAH-MEG. The PAM hydrogel (1 cm^2) was placed on the bottom Cu electrode along with the same-sized MXene aerogel, which stuck to the PAM hydrogel. The top Cu electrode was then placed on the top surface of the MXene aerogel.

Characterization. SEM (JEOL, 7001F) and EDS were employed to study the surfaces of the MXene aerogel and PAM hydrogel and to determine their elemental compositions, respectively. The N_2 adsorption/desorption curves and surface areas were measured using an Autosorb-iQ 2ST/MP (Quantachrome). The chemical compositions of the thin MXene films were determined using an XPS system (model K-Alpha, Thermo Scientific, USA). The contact angle was measured using an optical-contact-angle meter system (KRÜSS DSA 100, Germany). The zeta potential was measured using a ELS-1000ZS (Otsuka Electronics). The V_{oc} and J_{sc} of the MEGs were measured using a commercial multimeter, Keithley 6514 electrometer, and Keithley 6485 picoammeter. The RH was controlled in a humidity chamber composed of a humidifier and humidity sensor in an acrylic case. A refrigerator was used to establish below-freezing (–20 °C) and freezing (0 °C) conditions. The 20–80 °C experiments were carried out on a heating plate. KPFM characterization was performed using a Multimode 8 (TECSCO) with a 500 mV tip bias voltage. The CV curve of the MEGs was measured using a potentiostat/galvanostat (VMP3, Princeton Applied Research).

First principle simulation method

All our calculations were carried out by using density functional theory (DFT) with the generalized Perdew-Burke-Ernzerhof [1] and the projector-augmented wave (PAW) pseudopotential plane-wave method [2], as implemented in the VASP code [3]. For the PAW pseudopotentials, we included $3p^6 4s^2$, $2s^2 2p^5$, $3d^2 4s^2$, and $2s^2 2p^2$, as valence electrons for Ca, Cl, Ti and C, respectively. An 8 ×8 × 1 Γ-center k-point grid was used for Ti3C2 monolayer unit cell geometry optimizations and energy calculations, and a plane-wave basis set with an energy cutoff of 500 eV was adopted. Good convergence was obtained with these parameters, and the total energy was converged to 10−7 eV per atom, and the forces exerted on the atoms were less than 0.01 eV/Å. Spin polarization was considered in this study. The energy minimization was performed using a conjugate-gradient algorithm to relax the ions into their instantaneous ground state without

constraining lattice constants. The optimized T_3C_2 monolayer (a=b=3.105 Å) with a vacuum thickness of 20 Å was expended to 5×5×1 supercells for computing Ca and Cl diffusion energy barriers using the Nudged Elastic Band (NEB) method [4]. The vacancy formation energy E_f can be calculated using $E_f = E_{def} - (E_{per} - E_v)$. Here, E_{def} and E_{per} are the total energies of defective and perfect systems, respectively. E_v is the chemical potential of vacacy elements (Ti and C). It should be noted that the chemical potential of Ti or C has two boundary limits. Under Ti-rich and Ti-poor growth conditions, the chemical potential of Ti is taken from the metallic Ti and Ti_3C_2 compound, respectively. The charge density difference $\Delta\rho$ in Ca and Cladsorbed Ti_3C_2 surface is defined as $\Delta\rho = \rho_{A+C} - \rho_C - \rho_A$, where, ρ_{A+C}, ρ_C and ρ_A are the total charge density of Ca or Cl embedded Ti_3C_2, clean Ti_3C_2 system and ligands (Ca and Cl), respectively.

Author contributions

C.M.P. and K.Y.Z. conceived the concept and designed the experiments. K.Y.Z. and J.W.L. conducted experiments, data analysis, drawing figures, writing & reviewing and contributed equally to this work. Z.G.Y. and Y.-W. Z. contributed to DFT calculations and writing the DFT analysis. W.J. contributed to experiments designing and characterization. J.W.O. contributed to equipment setup and characterization. G.H.K. contributed to the schematic diagram drawing. H.W.H, Y.J.K., K.H.L, S.K.L, H.Y.K., T.B.K. and H.J.L contributed to characterization. C.E.L. contributed to hydrogel and organohydrogel fabrication. J.H.J and J.W.P. contributed for sensor performance measurement.

Conflicts of interest

The authors declare no competing interests.

Acknowledgements

This research was supported by the National Research Foundation of Korea (NRF) as a Creative Materials Discovery Program funded by the Ministry of Science and ICT (Grant No. NRF-2018M3D1A1058536) and the Korean government (MEST) (Grant No. 2020R1A2B5B03002697); the Technology Innovation Programme (20012430), funded by the Ministry of Trade, Industry, & Energy (MOTIE, Korea); the KIST Institutional Program (project No. 2E31032-21-150); and the Korea Initiative for fostering the University of Research and Innovation (KIURI) Program of the National Research Foundation (NRF), funded by the Korean government (MSIT) (NRF- 2020M3H1A1077207). The use of computing resources at the A*STAR Computational Centre and National Supercomputer Centre, Singapore, is gratefully acknowledged.

References

1. H. Wang, T. He, X. Hao, Y. Huang, H. Yao, F. Liu, H. Cheng and L. Qu, *Nature Communications*, 2022, **13**.
2. J. Bae, M. S. Kim, T. Oh, B. L. Suh, T. G. Yun, S. Lee, K. Hur, Y. Gogotsi, C. M. Koo and I. D. Kim, *Energy & Environmental Science*, 2022, **15**, 123-135.
3. J. Tang, Y. Zhao, M. Wang, D. Wang, X. Yang, R. Hao, M. Wang, Y. Wang, H. He, J. H. Xin and S. Zheng, *Nat Commun*, 2022, **13**, 1291.
4. X. Wang, F. Lin, X. Wang, S. Fang, J. Tan, W. Chu, R. Rong, J. Yin, Z. Zhang, Y. Liu and W. Guo, *Chem Soc Rev*, 2022, **51**, 4902-4927.
5. J. Tan, S. Fang, Z. Zhang, J. Yin, L. Li, X. Wang and W. Guo, *Nat Commun*, 2022, **13**, 3643.
6. A. K. S. a. N. K. S. Ghosh, *Science*, 2003, **299**, 1042–1044.
7. K. Fan, X. K. Liu, Y. Liu, Y. Li, X. Y. Liu, W. Feng and X. Wang, *Nano Energy*, 2022, **91**.
8. F. Zhao, L. Wang, Y. Zhao, L. Qu and L. Dai, *Adv Mater*, 2017, **29**.
9. H. H. Cheng, Y. X. Huang, F. Zhao, C. Yang, P. P. Zhang, L. Jiang, G. Q. Shi and L. T. Qu, *Energy & Environmental Science*, 2018, **11**, 2839-2845.
10. T. Xu, X. Ding, C. Shao, L. Song, T. Lin, X. Gao, J. Xue, Z. Zhang and L. Qu, *Small*, 2018, **14**, e1704473.
11. H. Cheng, Y. Huang, L. Qu, Q. Cheng, G. Shi and L. Jiang, *Nano Energy*, 2018, **45**, 37-43.
12. Q. Tang and P. Yang, *Journal of Materials Chemistry A*, 2016, **4**, 9730-9738.
13. K. Liu, T. P. Ding, J. Li, Q. Chen, G. B. Xue, P. H. Yang, M. Xu, Z. L. Wang and J. Zhou, *Advanced Energy Materials*, 2018, **8**.
14. C. Liu, S. Wang, X. Wang, J. Mao, Y. Chen, N. X. Fang and S.-P. Feng, *Energy & Environmental Science*, 2022, **15**, 2489-2498.
15. T. Xu, X. T. Ding, Y. X. Huang, C. X. Shao, L. Song, X. Gao, Z. P. Zhang and L. T. Qu, *Energy & Environmental Science*, 2019, **12**, 972-978.
16. K. Zhang, L. Cai, A. Nilghaz, G. Chen, X. Wan and J. Tian, *Nano Energy*, 2022, **98**.
17. X. M. Liu, H. Y. Gao, J. E. Ward, X. R. Liu, B. Yin, T. D. Fu, J. H. Chen, D. R. Lovley and J. Yao, *Nature*, 2020, **578**, 550-+.
18. L. H. Li, S. J. Feng, Y. Y. Bai, X. Q. Yang, M. Y. Liu, M. M. Hao, S. Q. Wang, Y. Wu, F. Q. Sun, Z. Liu and T. Zhang, *Nature Communications*, 2022, **13**.
19. L. H. Li, S. W. Gao, M. M. Hao, X. Q. Yang, S. J. Feng, L. L. Li, S. Q. Wang, Z. P. Xiong, F. Q. Sun, Y. Li, Y. Y. Bai, Y. Y. Zhao, Z. K. Wang and T. Zhang, *Nano Energy*, 2021, **85**.
20. Y. Zhang, S. Guo, Z. G. Yu, H. Qu, W. Sun, J. Yang, L. Suresh, X. Zhang, J. J. Koh and S. C. Tan, *Adv Mater*, 2022, DOI: 10.1002/adma.202201228, e2201228.
21. S. Yang, X. Tao, W. Chen, J. Mao, H. Luo, S. Lin, L. Zhang and J. Hao, *Adv Mater*, 2022, DOI: 10.1002/adma.202200693, e2200693.
22. W. Y. He, H. Y. Wang, Y. X. Huang, T. C. He, F. Y. Chi, H. H. Cheng, D. Liu, L. M. Dai and L. T. Qu, *Nano Energy*, 2022, **95**.
23. J. X. Bai, Y. X. Huang, H. Y. Wang, T. L. Guang, Q. H. Liao, H. H. Cheng, S. H. Deng, Q. K. Li, Z. G. Shuai and L. T. Qu, *Advanced Materials*, 2022, **34**.
24. F. Zhao, H. Cheng, Z. Zhang, L. Jiang and L. Qu, *Adv Mater*, 2015, **27**, 4351-4357.
25. C. Yang, Y. Huang, H. Cheng, L. Jiang and L. Qu, *Adv Mater*, 2019, **31**, e1805705.
26. W. Yang, X. Li, X. Han, W. Zhang, Z. Wang, X. Ma, M. Li and C. Li, *Nano Energy*, 2020, **71**.
27. Y. X. Huang, H. H. Cheng, C. Yang, H. Z. Yao, C. Li and L. T. Qu, *Energy & Environmental Science*, 2019, **12**, 1848-1856.
28. J. Bae, T. G. Yun, B. L. Suh, J. Kim and I. D. Kim, *Energy & Environmental Science*, 2020, **13**, 527-534.
29. L. H. Li, M. M. Hao, X. Q. Yang, F. Q. Sun, Y. Y. Bai, H. Y. Ding, S. Q. Wang and T. Zhang, *Nano Energy*, 2020, **72**.
30. Y. S. Qin, Y. S. Wang, X. Y. Sun, Y. J. Li, H. Xu, Y. S. Tan, Y. Li, T. Song and B. Q. Sun, *Angewandte Chemie-International Edition*, 2020, **59**, 10619-10625.
31. D. R. He, Y. C. Yang, Y. Zhou, J. Y. Wan, H. A. Wang, X. Fan, Q. Li and H. H. Huang, *Nano Energy*, 2021, **81**.
32. P. D. Li, N. Su, Z. Y. Wang and J. S. Qiu, *Acs Nano*, 2021, **15**, 16811-16818.
33. S. Zheng, J. Y. Tang, D. Lv, M. Wang, X. Yang, C. S. Hou, B. Yi, G. Lu, R. R. Hao, M. Z. Wang, Y. L. Wang, H. Y. He and X. Yao, *Advanced Materials*, 2022, **34**.
34. P. He, R. Guo, K. Hu, K. Liu, S. Lin, H. Wu, L. Huang, L. Chen and Y. Ni, *Chemical Engineering Journal*, 2021, **414**.
35. Q. Wang, X. Pan, X. Wang, H. Gao, Y. Chen, L. Chen, Y. Ni, S. Cao and X. Ma, *Composites Part B: Engineering*, 2020, **197**.
36. J.-N. Ma, Y.-L. Zhang, Y.-Q. Liu, D.-D. Han, J.-W. Mao, J.-R. Zhang, W.-C. Zhao and H.-B. Sun, *Science Bulletin*, 2022, **67**, 501-511.
37. Y. Li, Y. Wu, B. Shao, Z. Song, Y. Wang, J. Qiao, J. Di, W. Wei, T. Song and B. Sun, *ACS Appl Mater Interfaces*, 2021, **13**, 17902-17909.
38. A. K. Fard, G. McKay, R. Chamoun, T. Rhadfi, H. Preud'Homme and M. A. Atieh, *Chemical Engineering Journal*, 2017, **317**, 331-342.
39. H. Liao, X. Guo, P. Wan and G. Yu, *Advanced Functional Materials*, 2019, **29**.
40. J. Chi, C. Liu, L. Che, D. Li, K. Fan, Q. Li, W. Yang, L. Dong, G. Wang and Z. L. Wang, *Adv Sci (Weinh)*, 2022, **9**, e2201586.
41. Y.-Z. Zhang, K. H. Lee, D. H. Anjum, R. Sougrat, Q. Jiang, H. Kim and H. N. Alshareef, *Science advances*, 2018, **4**, eaat0098.
42. Y. Deng, T. Shang, Z. Wu, Y. Tao, C. Luo, J. Liang, D. Han, R. Lyu, C. Qi, W. Lv, F. Kang and Q. H. Yang, *Adv Mater*, 2019, **31**, e1902432.
43. X. P. Li, X. Li, H. Li, Y. Zhao, W. Li, S. Yan and Z. Z. Yu, *Advanced Sustainable Systems*, 2021, **5**.

44. X. Zhu, F. Zhang, L. Zhang, L. Zhang, Y. Song, T. Jiang, S. Sayed, C. Lu, X. Wang, J. Sun and Z. Liu, *Advanced Functional Materials*, 2018, **28**.
45. C. E. Lee, T. H. Park, S. Mun, Y. Jung, S. Lee, J. Jang, D. Y. Ryu and C. Park, *Advanced Materials Technologies*, 2022, DOI: 10.1002/admt.202200385.